

Research Article

Flower-Like Mn-Doped CeO₂ Microstructures: Synthesis, Characterizations, and Catalytic Properties

Ling Liu,^{1,2} Jingjing Shi,³ Xiaojun Zhang,³ and Jianzhou Liu³

¹Key Laboratory of Coal-Based CO₂ Capture and Geological Storage of Jiangsu Province, China University of Mining and Technology, Xuzhou 221008, China

²Low Carbon Energy Institute, China University of Mining and Technology, Xuzhou 221008, China

³School of Chemical Engineering and Technology, China University of Mining and Technology, Xuzhou 221116, China

Correspondence should be addressed to Ling Liu; liuling@cumt.edu.cn

Received 14 September 2015; Revised 18 November 2015; Accepted 22 November 2015

Academic Editor: Hossein Kazemian

Copyright © 2015 Ling Liu et al. This is an open access article distributed under the Creative Commons Attribution License, which permits unrestricted use, distribution, and reproduction in any medium, provided the original work is properly cited.

Mn-doped CeO₂ flower-like microstructures have been synthesized by a facile method, involving the precipitation of metallic alkoxide precursor in a polyol process from the reaction of CeCl₃·7H₂O with ethylene glycol in the presence of urea followed by calcination. By introducing manganese ions, the composition can be freely manipulated. To investigate whether there was a hybrid synergic effect in CH₄ combustion reaction, further detailed characteristics of Mn-doped CeO₂ with various manganese contents were revealed by XRD, Raman, FT-IR, SEM, EDS, XPS, OSC, H₂-TPR, and N₂ adsorption-desorption measurements. The doping manganese is demonstrated to increase the storage of oxygen vacancy for CH₄ and enhance the redox capability, which can efficiently convert CH₄ to CO₂ and H₂O under oxygen-rich condition. The excellent catalytic performance of MCO-3 sample, which was obtained with the starting Mn/Ce ratios of 0.2 in the initial reactant compositions, is associated with the larger surface area and richer surface active oxygen species.

1. Introduction

Metal oxide is an important catalyst support in many catalytic reactions and serves especially as a substitute for the transitional noble catalyst in the activation of hydrocarbon. Recently, as an important functional metal oxide, CeO₂ has attracted increasing interest with respect to its tremendous applications in environmental catalysis due to its oxygen vacancy defects and high oxygen storage capacity associated with the facile Ce⁴⁺/Ce³⁺ redox cycle [1–4]. However, owing to the poor thermal stability, pure CeO₂ does not perform well in real catalysis. The addition of other metals (M = Cu, Co, Ni, etc.) into CeO₂ fluorite lattice has been proven to exhibit higher oxygen storage capacity and better catalytic property than pure CeO₂ [5–7]. In principle, the high activity of MO_x-CeO₂ is correlated with the synergistic effect between MO_x and CeO₂, which facilitates the electron exchanges between Mⁿ⁺/Mⁿ⁺¹ and Ce³⁺/Ce⁴⁺, with both components being significantly more readily reduced or oxidized than

the corresponding independent ones. Consequently, controllable synthesis of doped CeO₂ catalysts, which possess facile redox process and high concentration of oxygen vacancies, will be beneficial to the enhancement of catalytic activity.

In general, the activity of a catalyst is associated with various structural factors, such as chemical composition, surface modifications, specific surface area, surface oxygen vacancies, and preferential exposure of reactive facets [8–12]. As for a mixed oxide catalyst, the high activity and stability in the catalytic reaction are significantly affected by the dispersion of active component. The synthetic method is the critical factor to control the dispersion of active component. Therefore, the recent reports highlighted some new routes for the synthesis of doped CeO₂ catalysts, which produced high catalytic performance. For example, hollow and solid MnO_x-CeO₂ nanospheres have been synthesized with a supercritical antisolvent process and used for the selective catalytic reduction of NO with NH₃ [13]. CeO₂ doped with transition metal ions (Co²⁺ and Ni²⁺), and Co/Ni

binary-doped CeO₂ mesoporous hollow nanospheres were prepared by a one-step solvothermal method and showed strikingly higher catalytic activity, owing to the intrinsic surface defects of the samples [14]. Cu-doped CeO₂ spheres were prepared by a simple hydrothermal method and the excellent catalytic performance of Cu-doped (10 at.%) CeO₂ spheres is associated with the porous spherical structure, high redox capability, and high oxygen vacancy [15]. Mesoporous CuO-CeO₂ catalysts were prepared by a surfactant-assisted coprecipitation method and the precursors exerted a great influence on the properties of CuO-CeO₂ catalysts. However, to our knowledge, little attention has been paid to the synthesis of doped CeO₂ catalysts by a polyol-based precursor route [16].

Herein, we report the synthesis of Mn-doped CeO₂ flower-like microstructures via thermal decomposition of metallic alkoxide precursors, which were synthesized in ethylene glycol-mediated process. Preliminary CH₄ catalytic oxidation experiments indicated that the Mn-doped CeO₂ samples showed strikingly higher catalytic activity than pure CeO₂, owing to the rich surface active oxygen species and large surface area.

2. Materials and Methods

2.1. Synthesis. All chemicals and solvents were of analytical grade and used as received without further purification or modification. Mn-doped CeO₂ catalysts were synthesized by a facile polyol-based precursor and annealing method. The prepared catalysts were Mn-doped CeO₂ powder with the Mn/Ce molar ratios of 0.1, 0.15, 0.2, and 0.3. As to the synthesis of Mn-doped CeO₂ (marked as MCO-1, Mn:Ce = 0.1), typically, 0.04 g of Mn(CH₃COO)₂·4H₂O, 0.6 g of CeCl₃·7H₂O, 0.5 g of CO(NH₂)₂, and 2 g of poly(vinylpyrrolidone) (PVP; K-30) were dissolved into 50 mL of EG in a 150 mL round flask to form a clear solution. The resulting solution was then heated to 180°C under reflux and constant stirring. The clear solution became opaque after 20 min and the reaction was stopped after refluxing for 1 h. Upon finishing the reaction, the sample was allowed to cool naturally, after which the final product was collected by centrifugation and washed with absolute ethanol several times and then dried in air at 80°C. Thermal decomposition of the precursors was achieved in muffle furnace at a heating rate of 6°C/min up to 450°C maintained for 2 h in static air.

Mn-doped CeO₂ catalysts with different Mn contents (Mn:Ce = 0.15, 0.2, and 0.3, which were marked as MCO-2, MCO-3, and MCO-4, resp.) were prepared under identical conditions, in order to investigate the role of composition in the catalytic activities. For comparison, pure CeO₂ was also prepared.

2.2. Characterization. Phase purity was examined by X-ray diffraction (XRD) on a Bruker D8-Advance powder X-ray diffractometer with Cu K α radiation ($\lambda = 0.15418$ nm). The morphologies and structures of the products obtained were determined by an FEI Quanta 250 emission scanning electron microscope (SEM) equipped with an energy dispersive X-ray spectrometer (EDS). Fourier transform infrared (FT-IR)

spectra were recorded for samples using KBr pellet technique in the range of 400–4000 cm⁻¹ (Bruker VERTEX 80v). Raman spectra were obtained using a Bruker Senterra Raman spectrometer with a laser wavelength of 785 nm. Surface analysis was carried out with X-ray photoelectron spectroscopy (XPS, Thermo ESCALAB 250Xi) with a standard Al K α source. All binding energies were referenced to the C1s peak (284.8 eV) arising from surface hydrocarbons (or adventitious hydrocarbons). Measurement of specific surface area and analysis of porosity for the products were performed through measuring N₂ adsorption-desorption isotherms at 77 K with a Quantachrome NOVA-3000 system. Specific surface area and pore size were calculated by the BET (Brunauer-Emmett-Teller) method and the BJH (Barrett-Joyner-Halenda) method, respectively.

The oxygen storage capacity (OSC) experiments were performed on a PCA-1200 instrument by pulse technique. The samples were pretreated at 550°C in flowing H₂ for 45 min and then in flowing Ar for 20 min and subsequently cooled to 200°C in Ar atmosphere. The reduced samples were oxidized at 300°C with pulse of O₂ periodically at an interval of 3 min until a constant value being obtained for the peak intensity. The O₂-OSC values were determined by the amount of O₂ consumed during the O₂ pulse.

The temperature-programmed reduction measurements under a H₂ environment (H₂-TPR) were performed with a PCA-1200 instrument. Typically, the catalyst sample (30 mg) was pretreated under an O₂ stream at 300°C for 30 min. After the sample cooled to room temperature, a flow of H₂/Ar was introduced into the samples at a flow rate of 30 mL/min, and the temperature was increased to 900°C at a rate of 10°C/min.

2.3. Catalytic Tests. The activity measurements were carried out in a continuous flow fixed-bed microreactor at atmospheric pressure. In the experiments, 200 mg of catalyst was loaded into a stainless steel reactor with a gas mixture typically containing 1% CH₄, 21% O₂, and 78% N₂ at the flow rate of 23.4 mL/min and the space velocity of 4000 h⁻¹ in the temperature range from 250 to 500°C. A portion of the product stream was extracted periodically from the reactor with an automatic sampling valve and analyzed using a gas chromatograph with a thermal conductivity detector.

3. Results and Discussion

3.1. Characteristics of Mn-Doped CeO₂ Flower-Like Microstructures with Various Manganese Contents. To investigate whether there was a hybrid synergic effect in CH₄ combustion reaction, we acquired detailed information on the structure and local atomic composition of the Mn-doped ceria with various Mn contents. Fundamental characteristics of the samples were revealed by FT-IR, XRD, SEM, EDS, XPS, Raman, BET, OSC, and H₂-TPR.

A polyol-based precursor route was developed to synthesize the Mn-doped CeO₂ samples with various Mn contents. Figure 1 displays the typical FT-IR spectrum of the MCO-1 precursor. The vibrational bands of $\nu_a(\text{CH}_2)$ and $\nu_s(\text{CH}_2)$ at 2888 and 2844 cm⁻¹ as well as the strong peak of $\nu(\text{C-O})$

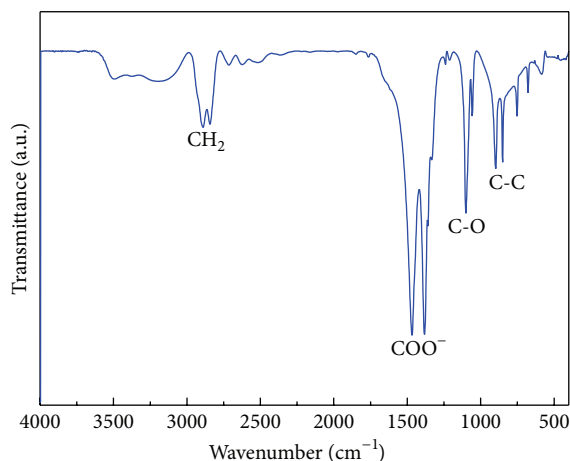


FIGURE 1: Typical FT-IR spectrum of the as-obtained MCO-1 precursor.

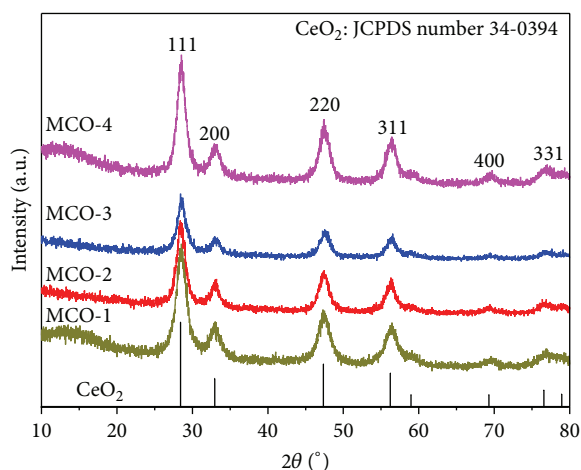


FIGURE 2: XRD patterns of Mn-doped CeO_2 samples with different Mn contents.

band at 1102 cm^{-1} derived from the ethylene glycol unit were observed, and the stretching vibrations of carboxylate group in acetate ions, $\nu_a(\text{COO}^-)$ and $\nu_s(\text{COO}^-)$, at 1465 and 1382 cm^{-1} were also detected. A broader band occurring at 3395 cm^{-1} can be attributed to the stretching vibration of OH groups linked by hydrogen bonds, and the band at 899 cm^{-1} can be viewed as $\nu(\text{C}-\text{C})$. Thus, we conclude that the precursor compound appears to be an alkoxide, which is similar to those previously reported metallic alkoxide precursors in ethylene glycol-mediated process [17–22].

XRD was employed to ascertain the change in bulk crystal structure for CeO_2 support. Figure 2 shows the XRD patterns of the Mn-doped CeO_2 samples with various Mn contents prepared by heat treatment of those precursors. The 2θ values were located at 28.5° , 33.1° , 47.4° , 56.2° , 59.0° , and 69.4° for the pure CeO_2 . It is clear that the diffraction peaks of all the samples correspond to the (111), (200), (220), and (311) planes that can be indexed to the cubic fluorite structure of CeO_2 crystals (JCPDS Card number 34-0394). The peak positions showed no critical change upon doping

TABLE 1: Lattice parameters and the proportions of O'' and Mn^{3+} of pure CeO_2 and Mn-doped CeO_2 samples calculated from XRD and XPS, respectively.

Samples	Lattice parameter (Å)	$\text{O}''/(\text{O}'' + \text{O}')$ (%)	$\text{Mn}^{3+}/(\text{Mn}^{2+} + \text{Mn}^{3+})$ (%)
Pure CeO_2	5.4113	39.5	—
MCO-1	5.4059	44.7	44.9
MCO-2	5.3983	45.4	45.1
MCO-3	5.3938	50.6	56.1
MCO-4	5.4015	45.9	56.8

with guest metals; and no peaks were observed corresponding to doped metal and other individual oxides. The peaks of MnO_x are not detected in the Mn-doped CeO_2 samples even when the amount of initial Mn content in the raw material reached up to 30 mol%, which indicates the existence of well dispersion of MnO_x species on the surface of CeO_2 and/or the incorporation of Mn into the CeO_2 lattice. However, the decrease of peak intensity and the slight increase of the peak width with the introduction of the dopant indicate that the grain sizes decrease after the metal ions are doped into the ceria. Moreover, as shown in Table 1, the lattice parameters obtained from the calculation of the (111) peak of Mn-doped CeO_2 are smaller than that of pure CeO_2 , which can prove that Mn atoms probably replace some of Ce sites and enter into the CeO_2 lattice [23]. Because the ionic radius of Mn^{n+} ($\text{Mn}^{4+} = 0.53\text{ Å}$, $\text{Mn}^{3+} = 0.645\text{ Å}$, and $\text{Mn}^{2+} = 0.83\text{ Å}$) is smaller than that of Ce^{4+} (1.01 Å), when Mn^{n+} embedded in CeO_2 lattice and takes the place of Ce^{4+} , the contraction and distortion of the ceria lattice occur, leading to the decrease of the cell parameter [24–26].

Raman scattering is an effective tool for the investigation of the effects of doping on nanomaterials, as the incorporation of dopants leads to shifts of the lattice Raman vibrational peak positions. Figure 3 displays the Raman spectra of pure CeO_2 as well as Mn-doped CeO_2 samples with different Mn contents. For the pure CeO_2 , a strong peak at 463 cm^{-1} can be assigned to the F_{2g} Raman active mode of the cubic fluorite structure of CeO_2 , which is due to the symmetric breathing mode of the oxygen atoms around cerium ions. The band at around 279 cm^{-1} can be related to the oxygen vacancies in CeO_2 lattice attributed to the presence of defective structure [13, 27]. Compared to the pure CeO_2 , the peak intensity decreased greatly and became broader and red-shifted for the Mn-doped CeO_2 . The red-shift could be attributed to the changes in lattice parameter with crystallite size, as it was previously reported that a decrease of the particle size of CeO_2 from $5\text{ }\mu\text{m}$ to 6.1 nm resulted in a shift to lower energy and was well explained by phonon confinement model [14, 28–30]. Additionally, the downshift is plausibly related to the presence of the Mn dopant, which would give rise to an increase in optical absorption [13, 31]. Another reason of shifting and broadening may be the increase in oxygen vacancies, which is related to structural defects derived from partially incorporation of manganese into CeO_2 lattice, in agreement

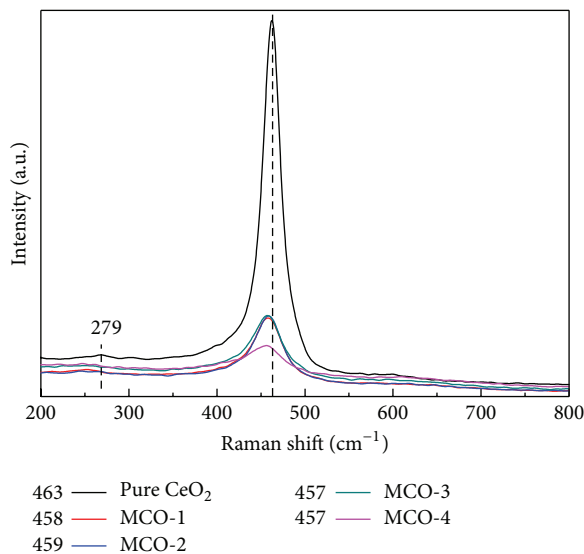


FIGURE 3: Raman spectra of pure CeO_2 and Mn-doped CeO_2 samples with different Mn contents. Peak positions (F_{2g}) are shown on the right.

with the decrease of lattice parameter [32]. In the Mn-doped ceria samples, the extra oxygen vacancies were generated by the incorporation of Mn ion into the ceria fluorite lattice to compensate for the valence mismatch between the Mn^{n+} and Ce^{4+} ions. One piece of supporting evidence for the possible increase of defect density is that the as-prepared pure CeO_2 sample shows a light yellow color, while the Mn-doped samples present various shades of taupe colors [14, 33].

The detailed morphologies and microstructures of the as-obtained Mn-doped CeO_2 with different Mn contents were characterized by SEM. As shown in Figure 4, the samples are composed of a great deal of flower-like architectures with a diameter of 2-3 μm , and the entire microstructure of the architecture was built from petals which connected with each other forming the flower-like microstructure by self-assembly. The results implied that doping Mn in CeO_2 did not change the total flower-like morphology. To determine the elemental compositions of the flower-like microstructures, EDS analysis has been carried out. The EDS spectrum and elemental mapping of the MCO-1 sample were depicted in Figure 5. Specifically, it appears that the pattern peaks of Mn, Ce, and O are clearly evident in the spectra collected, revealed the existence of the elements, and are accompanied with strong Au signals originated from gold plating on the sample before SEM examination. The elemental mapping results illustrate that the sample is mixed-metal oxide rather than a mixture of pure Mn and Ce phases. Moreover, the actual Mn/Ce ratios of the as-synthesized samples calculated from EDS are listed in Table 2. As can be seen, the actual Mn/Ce ratios in the products increased with the Mn/Ce ratios in the starting materials. The actual Mn/Ce ratios for the samples with the starting Mn/Ce ratios of 0.1, 0.15, 0.2, and 0.3 in the initial reactant compositions are 0.062, 0.070, 0.078, and 0.087, respectively. In the series of synthetic processes, the initial Mn/Ce molar ratio in the starting

TABLE 2: Actual Mn/Ce ratios of as-synthesized Mn-doped CeO_2 samples based on the EDS results.

Samples	MCO-1	MCO-2	MCO-3	MCO-4
Starting Mn/Ce ratio	0.1	0.15	0.2	0.3
Actual Mn/Ce ratio	0.062	0.070	0.078	0.087

materials did not totally coincide with that of these solid precipitation, and it is more likely to follow a curved relation for the powder synthesized in EG, which coincided with our previously reported results [18]. The EDS results indicate that the doped Mn contents are smaller than the initial reactant compositions; in other words, only a portion of the added Mn ions incorporate into the ceria lattice. This may be due to the large disparity of the ionic radii, which might make the insertion into the ceria lattice more difficult [34].

XPS was performed in order to further illuminate the surface composition and the chemical state of the elements existing in Mn-doped CeO_2 samples with various Mn contents. The XPS results suggest that the surface Mn/(Mn + Ce) ratios were rather low, even when the amount of initial Mn content in the raw material reached up to 30 mol% (surface Mn/(Mn + Ce) \approx 0.072), which coincided with the EDS results. As displayed in Figure 6(a), the two sets of spin-orbital multiplets, corresponding to the Ce $3d_{3/2}$ and Ce $3d_{5/2}$ contributions, are labeled as u and v [15, 35–37]. For $3d_{5/2}$ of Ce(IV), the Ce $3d^9 4f^2 L^{n-2}$ and Ce $3d^9 4f^1 L^{n-1}$ states form the peaks v and v'' , and the Ce $3d^9 4f^1 L^n$ state corresponds to the peak v''' . For $3d_{5/2}$ of Ce(III), the Ce $3d^9 4f^2 L^{n-1}$ and Ce $3d^9 4f^1 L^n$ states produce the peaks v° and v' . For Ce $3d_{3/2}$ labeled as u , the same assignment can be carried out. The result suggests that there is a certain amount of Ce^{3+} in all the Mn-doped CeO_2 samples.

The O 1s XPS spectra for the Mn-doped ceria samples early show the existence of two states of surface oxygen atoms (Figure 6(b)). The main peak O' at ca. 529.4 eV is characteristic of lattice oxygen atoms; an apparent shoulder peak O'' at ca. 531.3 eV has been assigned to oxide defects or absorbed oxygen ions with low coordination [13, 15, 16]. The strong peaks of the catalysts at 531.3 eV suggest that they are expected to have better oxygen storage capacity, which would be promising for their higher catalytic oxidation activity. As shown in Table 1, the ratio of O'' of the MCO-3 sample obviously increased (50.6%), indicating that the content of surface oxygen vacancy is increased by doping suitable amounts of Mn. However, the surface oxygen vacancy contents would be decreased with further increase in the Mn contents, which may be due to the formation of bulk MnO_x on the surface.

The Mn 2p XPS spectra of Mn-doped CeO_2 samples are displayed in Figure 6(c). The peaks are weak because of the low metal concentration of the surface elements; however, the compositions can still be identified in the spectra. The double peaks with binding energies of ca. 641.6 and 653.3 eV correspond to the characteristic of Mn $2p_{3/2}$ and Mn $2p_{1/2}$ signals, respectively [38, 39]. After refined fitting, the spectrum could be deconvoluted into four peaks. The peaks at 641.3 and 653.3 eV can be assigned to the presence

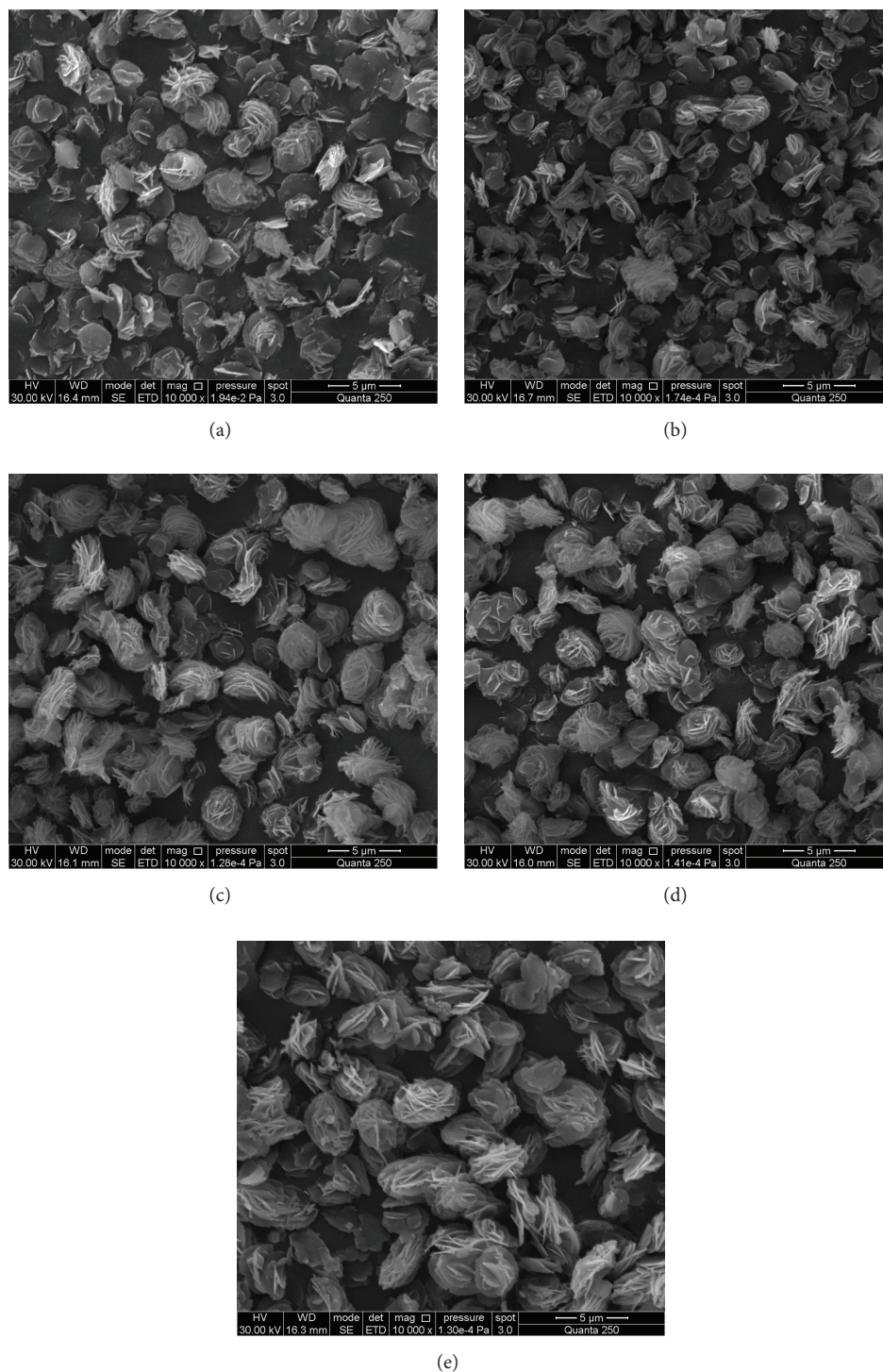


FIGURE 4: SEM images of the Mn-doped CeO₂ samples with different Mn contents: (a) MCO-1, (b) MCO-2, (c) MCO-3, and (d) MCO-4 and (e) pure CeO₂.

of Mn(II), while the other two peaks at 643.6 and 656.5 eV are characteristic of the Mn(III). This result suggests the coexistence of Mn²⁺/Mn³⁺ ion couple in the Mn-doped CeO₂ samples. The relative concentrations of Mn³⁺ are summarized in Table 1. It is obvious that the proportion of Mn³⁺ increases with the increase of Mn doping concentration.

As discussed above, the MCO-3 sample contains more amount of Mn³⁺ species and oxide defects (O^{''}), which are expected to exhibit different reduction properties and catalytic oxidation activities subsequently. These results provide an evidence of existence of redox equilibrium of Mn³⁺ + Ce³⁺ ↔ Mn²⁺ + Ce⁴⁺, which has been claimed to

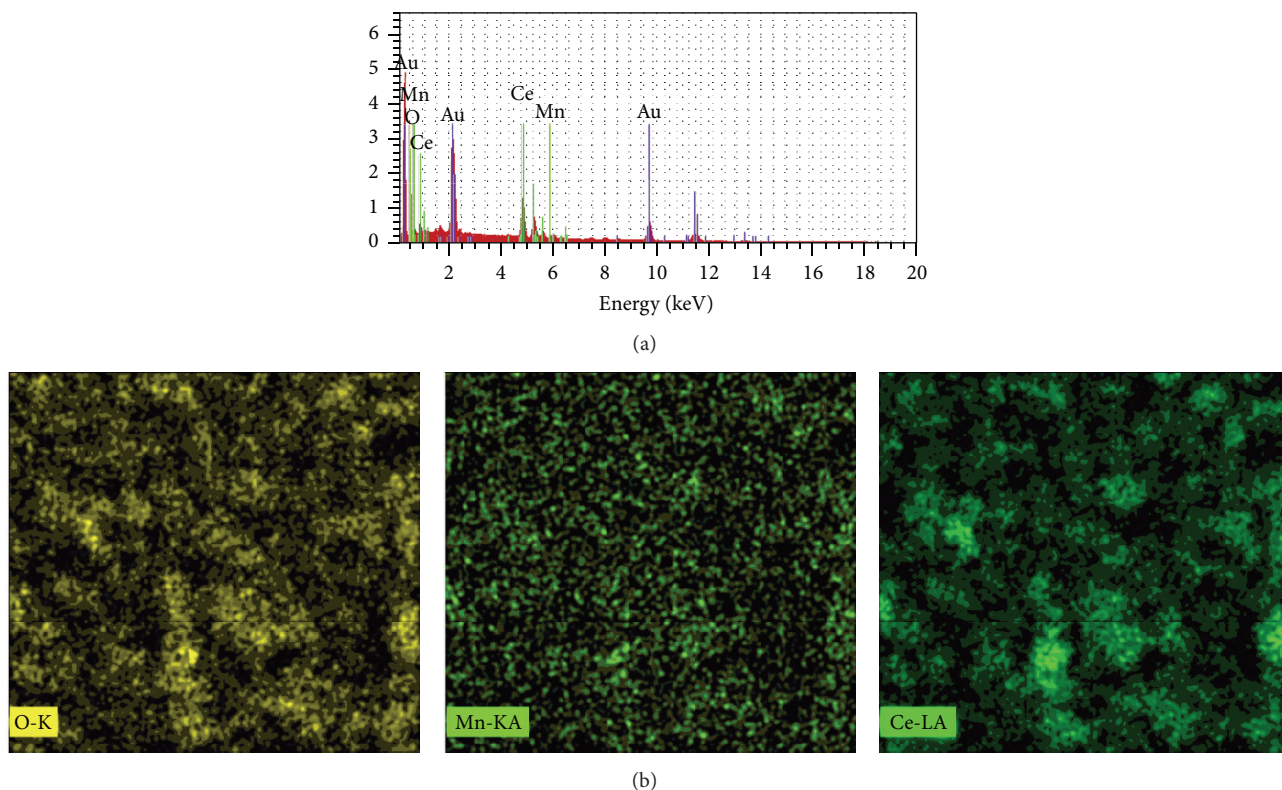


FIGURE 5: Typical EDS spectrum (a) and elemental mapping (b) of the as-synthesized MCO-1 sample.

TABLE 3: BET surface areas, average pore sizes, and total pore volumes of Mn-doped CeO_2 with various Mn contents.

Samples	BET surface area (m^2/g)	Average pore size (nm)	Total pore volume (cm^3/g)
MCO-1	56.0	13.04	0.100
MCO-2	75.7	8.12	0.085
MCO-3	91.0	7.90	0.109
MCO-4	74.2	16.64	0.167

be the source of a synergistic interaction between manganese and ceria species in the Mn-doped CeO_2 catalysts.

The textural properties of the as-synthesized Mn-doped CeO_2 samples were further investigated by measuring adsorption-desorption isotherms of N_2 at 77 K, as shown in Figure 7. The hysteresis features of these samples should be classified as type H3 loop, suggesting the presence of aggregates of plate-like particles which give rise to slit-shaped pores [10, 40]. The texture data of the series of the samples are summarized in Table 3. Herein, the specific surface areas using the BET method for these samples are 56.0, 75.7, 91.0, and $74.2 \text{ m}^2/\text{g}$, respectively. It was found that the MCO-3 sample exhibited higher BET surface area and smaller BJH pore size than those of the other Mn-doped CeO_2 samples. Thus, such high surface areas will undoubtedly benefit surface adsorption during catalytic reactions.

In redox catalysis, the role of ceria is usually to act as an oxygen transferring component. The oxygen storage capacity

TABLE 4: Oxygen storage capacity (OSC) of pure CeO_2 and Mn-doped CeO_2 with various Mn contents.

Samples	Pure CeO_2	MCO-1	MCO-2	MCO-3	MCO-4
OSC ($\mu\text{mol O}^2/\text{g}$)	89.5	111.5	133.0	166.2	155.4

(OSC) and the reducibility are important characteristics to determine its catalytic properties. The OSC results for all samples are displayed in Table 4. Obviously, all the three Mn-doped CeO_2 samples have much higher OSC than the pure CeO_2 . MCO-3 sample exhibited an OSC of $166.2 \mu\text{mol O}^2/\text{g}$, which is much higher than that of the other Mn-doped CeO_2 . These results are consistent with the Raman and XPS results evidencing structure defects. Previous studies have reported that the presence of defects in the structure and the exposure of more reactive crystallite planes at the surface should facilitate the formation of oxygen vacancies and enhance the OSC [41–43]. Therefore, the higher oxygen consumption is related to the defect density and the exposure of crystallite planes which is associated with the lower energy of formation of oxygen vacancies.

H_2 -TPR was performed to explore the oxygen reactivity and reducibility of the pure ceria and Mn-doped ceria. Generally, the reducibility of oxide is associated with the formation of oxygen vacancies: the more susceptible reducible an oxide is, the easier it can generate oxygen vacancies [11]. The H_2 consumption profiles as a function of temperature for all of

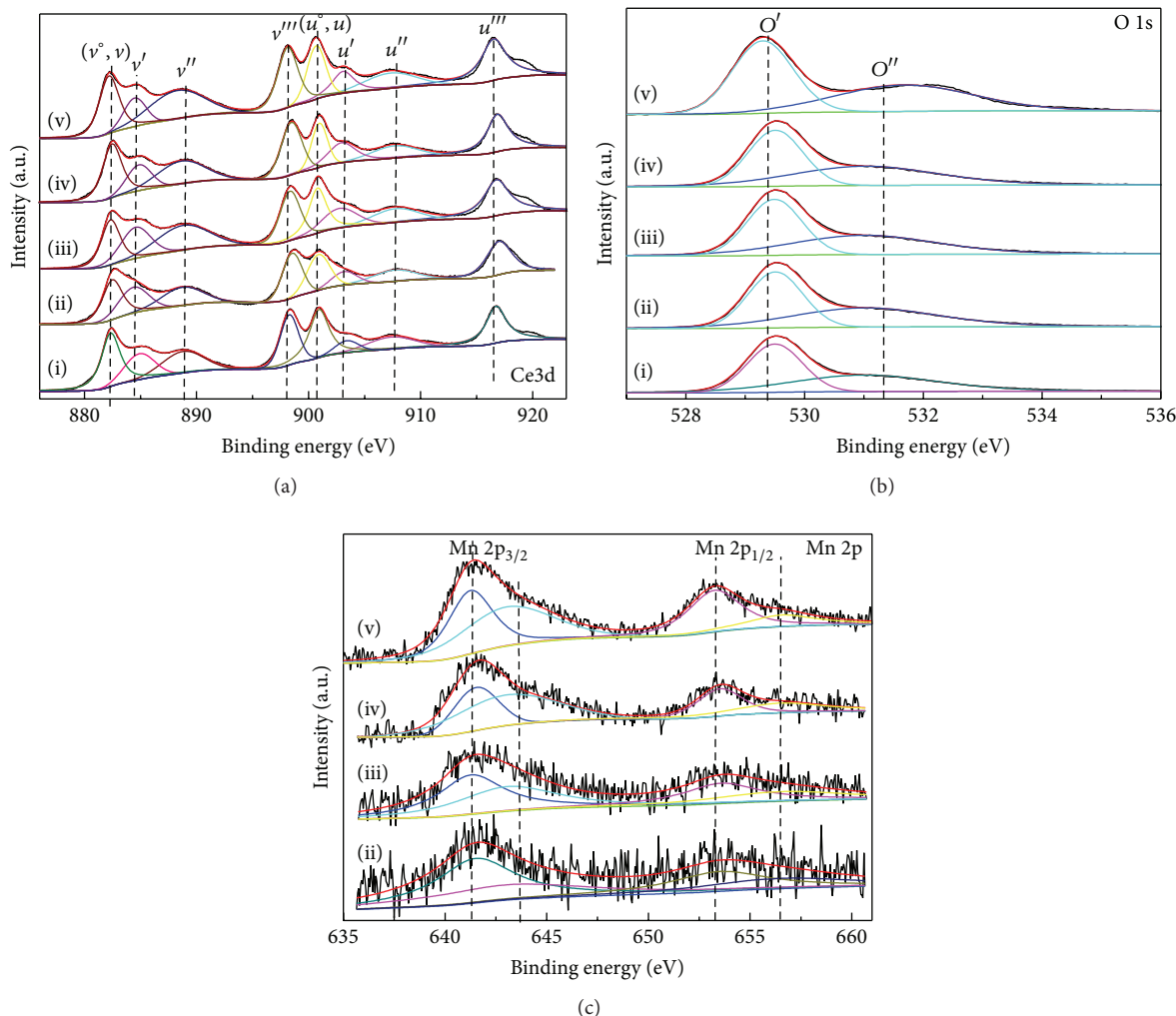


FIGURE 6: XPS region spectra of (a) Ce 3d, (b) O 1s, and (c) Mn 2p for pure CeO₂ (i) and Mn-doped CeO₂ samples with different Mn contents: (ii) MCO-1, (iii) MCO-2, (iv) MCO-3, and (v) MCO-4.

the samples are shown in Figure 8. The reduction behavior of pure CeO₂ was divided into two steps: the α peak at lower temperature (350–550°C) is due to the reduction of surface oxygen of CeO₂, and the β peak at higher temperature (ca. 820°C) is due to the reduction ($\text{Ce}^{4+} \rightarrow \text{Ce}^{3+}$) of bulk CeO₂ [12–16, 25–28]. The β peak of bulk CeO₂ reduction was commonly observed at around 820°C, with no significant change being observed for any samples. However, the α peak of surface reduction was changed significantly upon Mn doping, and new peak (γ) has appeared below 300°C due to the reduction of doped Mn element ($\text{Mn}^{3+} \rightarrow \text{Mn}^{2+}$) [13]. Owing to the doping with Mn element, the α peaks are shifted to lower temperature, and the peak areas increase. In the MCO-3 and MCO-4 samples, the α peaks are around 376°C, which are lower than those of MCO-1 (415°C) and MCO-2 (406°C) samples. Additionally, the γ peak of MCO-4 sample is at 261°C, while the γ peak shifts to the lower temperature (238°C). Therefore, it is obvious that the MCO-3 sample shows high redox properties at the lowest temperature among Mn-doped CeO₂ samples with various

manganese contents. From these observations, it is evident that when Mn ions are doped into the ceria, the surface oxygen concentration has been improved as more oxygen vacancies are produced. This is good in agreement with the results of the Raman, XPS, and OSC analyses. Therefore, a higher concentration of these surface defects can be expected for Mn-doped ceria. It is generally known that ceria can trap and release oxygen via the transformation between Ce^{3+} and Ce^{4+} . When Mn dopant was incorporated, the Mn-doped CeO₂ samples can easily trap and release oxygen via the interaction between $\text{Mn}^{3+}/\text{Mn}^{2+}$ and $\text{Ce}^{4+}/\text{Ce}^{3+}$, and simultaneously the surface oxygen can participate in the CH₄ catalytic oxidation. Consequently, the MCO-3 sample may exhibit an excellent catalytic performance at the lowest temperature as a result of the highest redox properties, which will also be verified by the catalytic activity evaluation in the following text.

3.2. Catalytic Performance of Mn-Doped CeO₂ Flower-Like Microstructures with Various Manganese Contents. Catalytic

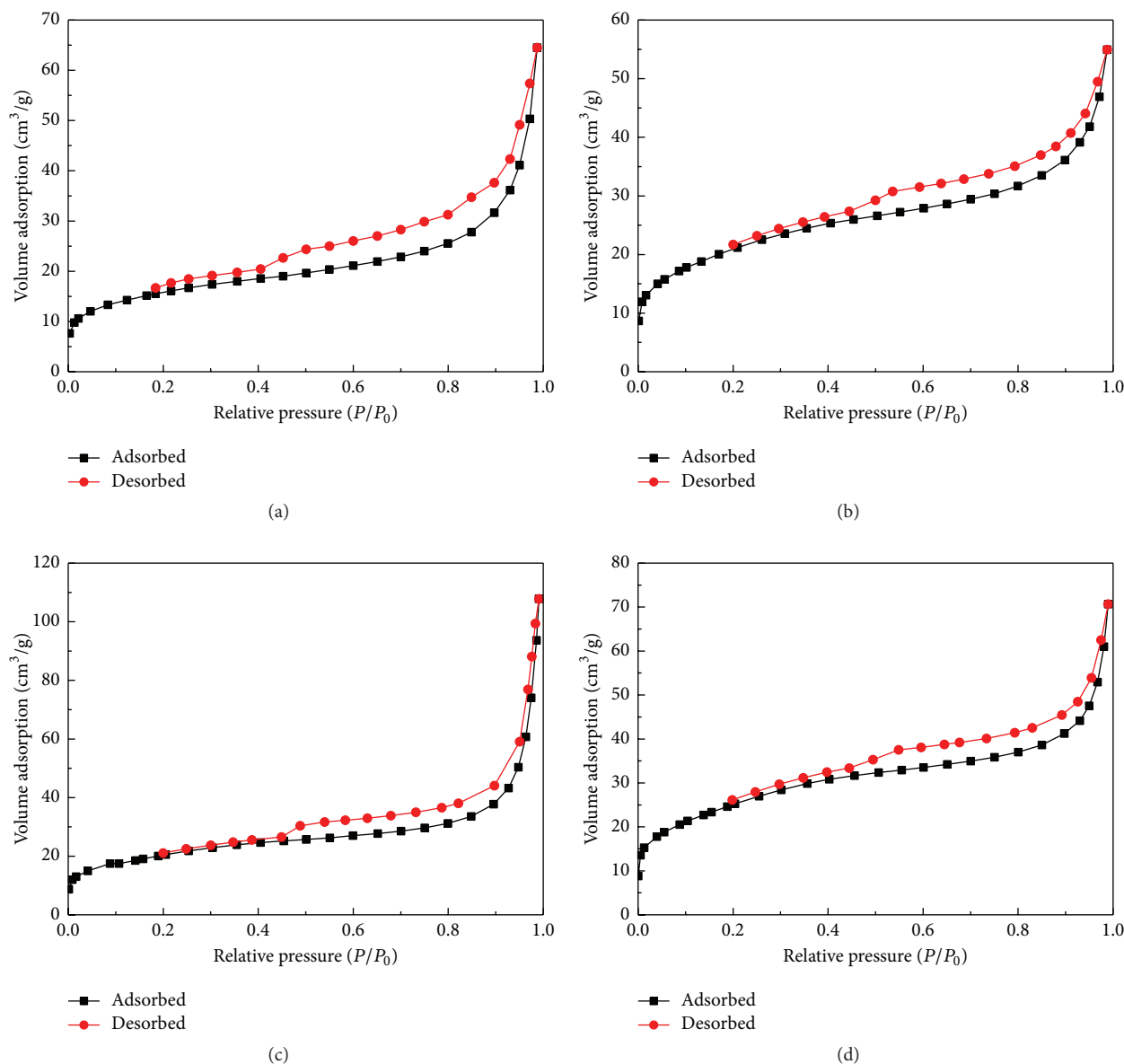


FIGURE 7: The N_2 adsorption-desorption isotherms of Mn-doped CeO_2 catalysts with various Mn contents: (a) MCO-1, (b) MCO-2, (c) MCO-3, and (d) MCO-4.

oxidation of CH_4 to CO_2 and H_2O under oxygen-rich condition plays an important role in energy supply using natural gas and here is used as a probe reaction to evaluate the catalytic performance of the Mn-doped CeO_2 samples. Figure 9(a) shows the CH_4 conversions at various temperatures over Mn-doped CeO_2 with various Mn contents. It is obvious that Mn-doped CeO_2 samples display enhanced catalytic activity for CH_4 oxidation, which is more active than that of pure CeO_2 . It is worth noting that the MCO-3 sample has higher activity than the catalysts with higher or lower Mn content. The reaction temperatures at CH_4 conversions of T_{10} and T_{50} are summarized in Table 5. The value of T_{10} and T_{50} in the MCO-3 sample is 339 and 405°C, respectively, which is much lower than that of the other Mn-doped CeO_2 samples; and T_{90} was observed at 457°C

for the MCO-3 sample. The results show that adding Mn in CeO_2 can obviously promote the catalytic activity of the Mn-doped CeO_2 , which could be interpreted in terms of the facile reduction property induced by adding Mn in CeO_2 . Kinetic studies have shown that the reaction mechanism of CH_4 oxidation over metal oxide nanocrystals is the Mars-van Krevelen redox model. The reoxidation of the reduced metal oxide sites by the gaseous oxygen is the rate-limiting step [12, 44]. High bulk oxygen mobility and formation of highly active oxygen species activated by the oxygen vacancies are widely recognized as the main factors influencing the catalytic activity of binary oxides for CH_4 catalytic oxidation activity [12]. In our work, the improvement in catalytic activity can be attributed to the incorporation of extraneous atoms into CeO_2 fluorite lattice. The interaction between

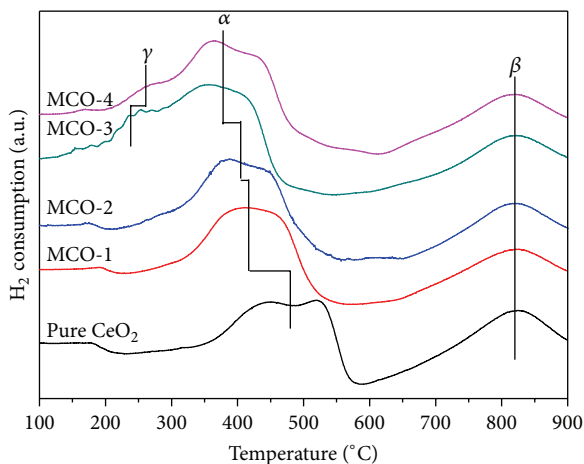


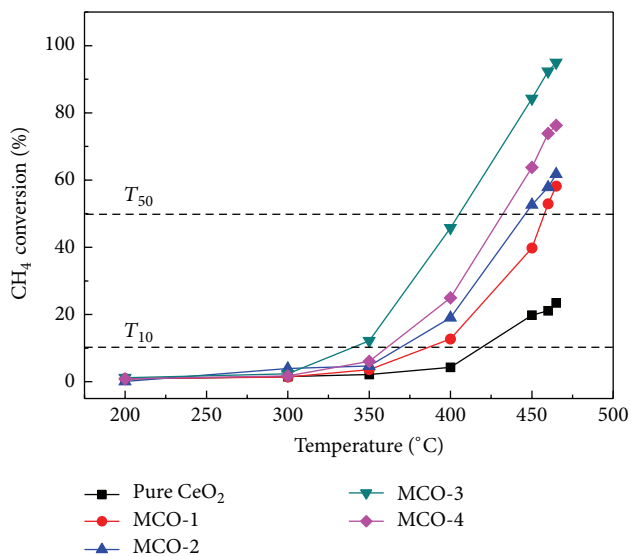
FIGURE 8: H_2 -TPR profiles of pure CeO_2 and Mn-doped CeO_2 catalysts with different Mn contents.

Mn^{2+}/Mn^{3+} and Ce^{3+}/Ce^{4+} couples takes place at boundaries of ceria, which leads to the valence changes of manganese species [13, 45, 46]. After a small amount of Mn ions is introduced into the CeO_2 lattice, the replacement of Mn^{n+} for Ce^{4+} results in a slight lattice contraction in the ceria lattice due to the smaller size of Mn ion and, more importantly, the generation of oxygen vacancies for charge compensation. Thus free oxygen molecules in reactant gas would be captured by these oxygen vacancies in the CeO_2 lattice to form active oxygen species, leading to more adsorbed reactant molecules being oxidized to CO_2 in turn. From the characterization and calculation results, the MCO-3 sample has a higher surface area, providing easily accessible pores for gas diffusion, which also favors the efficient oxidation of CH_4 . Moreover, higher oxygen mobility and richer surface active oxygen species are achieved in the MCO-3 sample. These are beneficial to the oxidation-reduction reaction. These are the reasons why the MCO-3 sample shows a better catalytic performance.

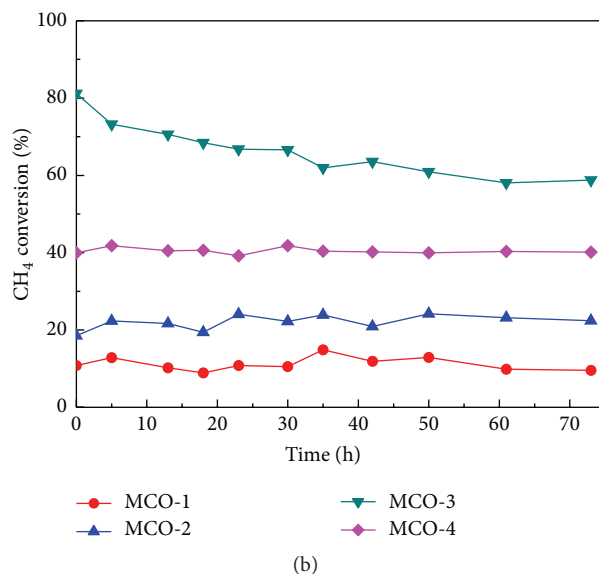
Catalytic stabilities for CH_4 oxidation were further investigated over these Mn-doped CeO_2 samples at $450^\circ C$ for 82 h. As shown in Figure 9(b), the CH_4 conversion over the MCO-3 sample is 80% during the first run and then tended to decrease, but it is still kept above 60% after 82 h on stream. The reason for deactivation could be attributed to the coke formation and/or the textural changes at high temperatures which could decrease the active sites. More work is underway to determine the underlying catalytic mechanism and the reason for deactivation of the doped ceria microstructures, and the result will be reported elsewhere. However, it can be seen from the CH_4 conversion versus time on stream curves that the other three Mn-doped CeO_2 samples demonstrate robust long-term stabilities with less than 5% changes relative in the absolute CH_4 conversions after 82 h on stream.

4. Conclusions

In summary, Mn-doped CeO_2 flower-like microstructures have been successfully synthesized via a polyol-based precursor process at $180^\circ C$ and subsequent direct thermal



(a)



(b)

FIGURE 9: (a) Plots of CH_4 conversion versus temperature over pure CeO_2 and Mn-doped CeO_2 with various manganese contents; (b) catalytic stability test of Mn-doped CeO_2 with various manganese contents.

TABLE 5: The reaction temperatures at CH_4 conversions of 10% (T_{10}) and 50% (T_{50}).

Samples	Pure CeO_2	MCO-1	MCO-2	MCO-3	MCO-4
T_{10} ($^\circ C$)	418	387	370	339	360
T_{50} ($^\circ C$)	—	457	446	405	432

decomposition at $450^\circ C$. The resultant samples were used as catalysts in CH_4 combustion under oxygen-rich condition. Catalytic results suggest that the Mn-doped CeO_2 show relatively higher activity. The fundamental characteristics of the Mn-doped CeO_2 samples with different Mn contents were revealed to investigate whether there was a hybrid

synergic effect in CH₄ combustion reaction. SEM results reveal that the doping Mn ions in CeO₂ did not change the total flower-like morphology. BET, XPS, OSC, and H₂-TPR results suggest that the higher surface area, more Mn³⁺, richer surface active oxygen species, and higher bulk oxygen mobility are responsible for the better performance of the MCO-3 sample. The as-obtained doped CeO₂ should be a promising material for environmental application and is expected to be useful in many other application fields. It is also believed that this synthetic method may provide a powerful synthetic technology for the future application of binary/ternary metal oxide nano/microstructures.

Conflict of Interests

The authors declare that there is no conflict of interests regarding the publication of this paper.

Acknowledgments

This work was financially supported by the National Natural Science Foundation of China (NSFC) (21306223) and the Fundamental Research Funds for the Central Universities (2012QNA09).

References

- W. Q. Shi, Y. Z. Li, J. T. Hou et al., "Densely populated mesopores in microcuboid CeO₂ crystal leading to a significant enhancement of catalytic activity," *Journal of Materials Chemistry A*, vol. 1, no. 3, pp. 728–734, 2013.
- T. T. Nguyen, P. T. M. Pham, T. M. Le, and I. V. Driessche, "Co₃O₄ catalysts on CeO₂-ZrO₂ supports and Co₃O₄-CeO₂ catalysts on Al₂O₃/SiO₂ supports for the oxidation of propylene," *Journal of Chemistry*, vol. 2015, Article ID 912905, 8 pages, 2015.
- Y. Park, S. K. Kim, D. Pradhan, and Y. Sohn, "Surface treatment effects on CO oxidation reactions over Co, Cu, and Ni-doped and codoped CeO₂ catalysts," *Chemical Engineering Journal*, vol. 250, pp. 25–34, 2014.
- J. W. Qin, J. F. Lu, M. H. Cao, and C. W. Hu, "Synthesis of porous CuO-CeO₂ nanospheres with an enhanced low-temperature CO oxidation activity," *Nanoscale*, vol. 2, no. 12, pp. 2739–2743, 2010.
- F. Esch, S. Fabris, L. Zhou et al., "Electron localization determines defect formation on ceria substrates," *Science*, vol. 309, no. 5735, pp. 752–755, 2005.
- K. B. Zhou, X. Wang, X. M. Sun, Q. Peng, and Y. D. Li, "Enhanced catalytic activity of ceria nanorods from well-defined reactive crystal planes," *Journal of Catalysis*, vol. 229, no. 1, pp. 206–212, 2005.
- F. Larachi, J. Pierre, A. Adnot, and A. Bernis, "Ce 3d XPS study of composite Ce_xMn_{1-x}O_{2-y} wet oxidation catalysts," *Applied Surface Science*, vol. 195, no. 1–4, pp. 236–250, 2002.
- L. H. Hu, Q. Peng, and Y. D. Li, "Selective synthesis of Co₃O₄ nanocrystal with different shape and crystal plane effect on catalytic property for methane combustion," *Journal of the American Chemical Society*, vol. 130, no. 48, pp. 16136–16137, 2008.
- C.-A. Wang, S. Li, and L. N. An, "Hierarchically porous Co₃O₄ hollow spheres with tunable pore structure and enhanced catalytic activity," *Chemical Communications*, vol. 49, no. 67, pp. 7427–7429, 2013.
- C. C. Li, X. M. Yin, T. H. Wang, and H. C. Zeng, "Morphogenesis of highly uniform CoCO₃ submicrometer crystals and their conversion to mesoporous Co₃O₄ for gas-sensing applications," *Chemistry of Materials*, vol. 21, no. 20, pp. 4984–4992, 2009.
- Z. Y. Fei, S. C. He, L. Li, W. J. Ji, and C.-T. Au, "Morphology-directed synthesis of Co₃O₄ nanotubes based on modified Kirkendall effect and its application in CH₄ combustion," *Chemical Communications*, vol. 48, no. 6, pp. 853–855, 2012.
- L. F. Liotta, H. Wu, G. Pantaleo, and A. M. Venezia, "Co₃O₄ nanocrystals and Co₃O₄-MO_x binary oxides for CO, CH₄ and VOC oxidation at low temperatures: a review," *Catalysis Science & Technology*, vol. 3, no. 12, pp. 3085–3102, 2013.
- D. Y. Jiang, M. H. Zhang, G. M. Li, and H. X. Jiang, "Preparation and evaluation of MnO_x-CeO₂ nanospheres via a green route," *Catalysis Communications*, vol. 17, pp. 59–63, 2012.
- X. F. Liu, L. Han, W. Liu, and Y. Z. Yang, "Synthesis of Co/Ni unitary- or binary-doped CeO₂ mesoporous nanospheres and their catalytic performance for CO oxidation," *European Journal of Inorganic Chemistry*, vol. 2014, no. 31, pp. 5370–5377, 2014.
- D. S. Zhang, Y. L. Qian, L. Y. Shi et al., "Cu-doped CeO₂ spheres: synthesis, characterization, and catalytic activity," *Catalysis Communications*, vol. 26, pp. 164–168, 2012.
- L. Qi, Q. Yu, Y. Dai et al., "Influence of cerium precursors on the structure and reducibility of mesoporous CuO-CeO₂ catalysts for CO oxidation," *Applied Catalysis B: Environmental*, vol. 119–120, pp. 308–320, 2012.
- L. Liu and Y. Z. Yang, "Shape-controlled synthesis of Mn-Co complex oxide nanostructures via a polyol-based precursor route and their catalytic properties," *Superlattices and Microstructures*, vol. 54, no. 1, pp. 26–38, 2013.
- X. F. Song and L. Gao, "Facile synthesis and hierarchical assembly of hollow nickel oxide architectures bearing enhanced photocatalytic properties," *The Journal of Physical Chemistry C*, vol. 112, no. 39, pp. 15299–15305, 2008.
- L.-S. Zhong, J.-S. Hu, H.-P. Liang, A.-M. Cao, W.-G. Song, and L.-J. Wan, "Self-assembled 3D flowerlike iron oxide nanostructures and their application in water treatment," *Advanced Materials*, vol. 18, no. 18, pp. 2426–2431, 2006.
- A.-M. Cao, J.-S. Hu, H.-P. Liang et al., "Hierarchically structured cobalt oxide (Co₃O₄): the morphology control and its potential in sensors," *The Journal of Physical Chemistry B*, vol. 110, no. 32, pp. 15858–15863, 2006.
- N. Chakroune, G. Viau, S. Ammar et al., "Synthesis, characterization and magnetic properties of disk-shaped particles of a cobalt alkoxide: CoII(C₂H₄O₂)," *New Journal of Chemistry*, vol. 29, no. 2, pp. 355–361, 2005.
- L. Liu, X. J. Zhang, and J. Z. Liu, "Facile synthesis of Mn-Co oxide nanospheres with controllable interior structures and their catalytic properties for methane combustion," *Materials Letters*, vol. 136, pp. 209–213, 2014.
- G. Avgouropoulos, T. Ioannides, and H. Matralis, "Influence of the preparation method on the performance of CuO-CeO₂ catalysts for the selective oxidation of CO," *Applied Catalysis B: Environmental*, vol. 56, no. 1–2, pp. 87–93, 2005.
- L. M. Shi, W. Chu, F. F. Qu, and S. H. Luo, "Low-temperature catalytic combustion of methane over MnO_x-CeO₂ mixed oxide catalysts: effect of preparation method," *Catalysis Letters*, vol. 113, no. 1–2, pp. 59–64, 2007.

- [25] X. F. Tang, Y. G. Li, X. M. Huang et al., "MnO_x-CeO₂ mixed oxide catalysts for complete oxidation of formaldehyde: effect of preparation method and calcination temperature," *Applied Catalysis B: Environmental*, vol. 62, no. 3-4, pp. 265-273, 2006.
- [26] B. Murugan, A. V. Ramaswamy, D. Srinivas, C. S. Gopinath, and V. Ramaswamy, "Nature of manganese species in Ce_{1-x}Mn_xO_{2-δ} solid solutions synthesized by the solution combustion route," *Chemistry of Materials*, vol. 17, no. 15, pp. 3983-3993, 2005.
- [27] Z.-Y. Pu, J.-Q. Lu, M.-F. Luo, and Y.-L. Xie, "Study of oxygen vacancies in Ce_{0.9}Pr_{0.1}O_{2-δ} solid solution by in situ X-ray diffraction and in situ raman spectroscopy," *The Journal of Physical Chemistry C*, vol. 111, no. 50, pp. 18695-18702, 2007.
- [28] J. E. Spanier, R. D. Robinson, F. Zhang, S. W. Chan, and I. P. Herman, "Size-dependent properties of CeO_{2-y} nanoparticles as studied by Raman scattering," *Physical Review B*, vol. 64, no. 24, Article ID 245407, pp. 245407-245411, 2001.
- [29] I. Kosacki, T. Suzuki, H. U. Anderson, and P. Colomban, "Raman scattering and lattice defects in nanocrystalline CeO₂ thin films," *Solid State Ionics*, vol. 149, no. 1-2, pp. 99-105, 2002.
- [30] M. Fernández-García, A. Martínez-Arias, J. C. Hanson, and J. A. Rodriguez, "Nanostructured oxides in chemistry: characterization and properties," *Chemical Reviews*, vol. 104, no. 9, pp. 4063-4104, 2004.
- [31] D. Gamarra, G. Munuera, A. B. Hungría et al., "Structure-activity relationship in nanostructured copper-ceria-based preferential CO oxidation catalysts," *The Journal of Physical Chemistry C*, vol. 111, no. 29, pp. 11026-11038, 2007.
- [32] L. Ilieva, G. Pantaleo, I. Ivanov, A. M. Venezia, and D. Andreeva, "Gold catalysts supported on CeO₂ and CeO₂-Al₂O₃ for NO_x reduction by CO," *Applied Catalysis B: Environmental*, vol. 65, no. 1-2, pp. 101-109, 2006.
- [33] A. S. Singhal, S. N. Achary, J. Manjanna, O. D. Jayakumar, R. M. Kadam, and A. K. Tyagi, "Colloidal Fe-doped indium oxide nanoparticles: facile synthesis, structural, and magnetic properties," *The Journal of Physical Chemistry C*, vol. 113, no. 9, pp. 3600-3606, 2009.
- [34] W.-T. Chen, K.-B. Chen, M.-F. Wang, S.-F. Weng, C.-S. Lee, and M. C. Lin, "Enhanced catalytic activity of Ce_{1-x}M_xO₂ (M=Ti, Zr, and Hf) solid solution with controlled morphologies," *Chemical Communications*, vol. 46, no. 19, pp. 3286-3288, 2010.
- [35] L.-S. Zhong, J.-S. Hu, A.-M. Cao, Q. Liu, W.-G. Song, and L.-J. Wan, "3D flowerlike ceria micro/nanocomposite structure and its application for water treatment and CO removal," *Chemistry of Materials*, vol. 19, no. 7, pp. 1648-1655, 2007.
- [36] C. M. Ho, J. C. Yu, T. Kwong, A. C. Mak, and S. Y. Lai, "Morphology-controllable synthesis of mesoporous CeO₂ nano- and microstructures," *Chemistry of Materials*, vol. 17, no. 17, pp. 4514-4522, 2005.
- [37] A. E. Nelson and K. H. Schulz, "Surface chemistry and microstructural analysis of Ce_xZr_{1-x}O_{2-y} model catalyst surfaces," *Applied Surface Science*, vol. 210, no. 3-4, pp. 206-221, 2003.
- [38] K. Ramesh, L. W. Chen, F. X. Chen, Y. Liu, Z. Wang, and Y.-F. Han, "Re-investigating the CO oxidation mechanism over unsupported MnO, Mn₂O₃ and MnO₂ catalysts," *Catalysis Today*, vol. 131, no. 1-4, pp. 477-482, 2008.
- [39] Y.-F. Han, F. X. Chen, Z. Y. Zhong, K. Ramesh, L. W. Chen, and E. Widjaja, "Controlled synthesis, characterization, and catalytic properties of Mn₂O₃ and Mn₃O₄ nanoparticles supported on mesoporous silica SBA-15," *The Journal of Physical Chemistry B*, vol. 110, no. 48, pp. 24450-24456, 2006.
- [40] K. S. W. Sing, D. H. Everett, R. A. W. Haul et al., "Reporting physisorption data for gas/solid system with special reference to determination of surface area and porosity," *Pure and Applied Chemistry*, vol. 57, no. 11, pp. 603-619, 1985.
- [41] D. Wang, Y. Kang, V. Doan-Nguyen et al., "Synthesis and oxygen storage capacity of two-dimensional ceria nanocrystals," *Angewandte Chemie*, vol. 50, no. 19, pp. 4378-4381, 2011.
- [42] H.-X. Mai, L.-D. Sun, Y.-W. Zhang et al., "Shape-selective synthesis and oxygen storage behavior of ceria nanopolyhedra, nanorods, and nanocubes," *The Journal of Physical Chemistry B*, vol. 109, no. 51, pp. 24380-24385, 2005.
- [43] R. C. R. Neto and M. Schmal, "Synthesis of CeO₂ and CeZrO₂ mixed oxide nanostructured catalysts for the iso-syntheses reaction," *Applied Catalysis A: General*, vol. 450, pp. 131-142, 2013.
- [44] N. Bahlawane, "Kinetics of methane combustion over CVD-made cobalt oxide catalysts," *Applied Catalysis B: Environmental*, vol. 67, no. 3-4, pp. 168-176, 2006.
- [45] G. Qi, R. T. Yang, and R. Chang, "MnO_x-CeO₂ mixed oxides prepared by co-precipitation for selective catalytic reduction of NO with NH₃ at low temperatures," *Applied Catalysis B: Environmental*, vol. 51, no. 2, pp. 93-106, 2004.
- [46] A. Martínez-Arias, A. B. Hungría, G. Munuera, and D. Gamarra, "Preferential oxidation of CO in rich H₂ over CuO/CeO₂: details of selectivity and deactivation under the reactant stream," *Applied Catalysis B: Environmental*, vol. 65, no. 3-4, pp. 207-216, 2006.



Hindawi

Submit your manuscripts at
<http://www.hindawi.com>

